SANDIA REPORT

SAND99-0111
Unlimited Release
Printed January 1999

Automation, Control, and Modeling of Compound Semiconductor Thin-Film Growth

Michael E. Coltrin, John F. Klem, Hong Q. Hou, W. G. Breiland, Timothy J. Drummond, Kevin M. Horn, Jeffrey Y. Tsao

Prepared by
Sandia National Laboratories
Albuquerque, New Mexico 87185 and Livermore, California 94550

Sandia is a multiprogram laboratory operated by Sandia Corporation, a Lockheed Martin Company, for the United States Department of Energy under Contract DE-AC04-94AL85000.

Sandia National Laboratories

Issued by Sandia National Laboratories, operated for the United States Department of Energy by Sandia Corporation.

Available to DOE and DOE contractors from
Office of Scientific and Technical Information
P.O. Box 62
Oak Ridge, TN 37831

Prices available from (703) 605-6000
Web site: http://www.ntis.gov/ordering.htm

Available to the public from
National Technical Information Service
U.S. Department of Commerce
5285 Port Royal Rd
Springfield, VA 22161

NTIS price codes
Printed copy: A03
Microfiche copy: A01

DISCLAIMER

Portions of this document may be illegible in electronic image products. Images are produced from the best available original document.

SAND99-0111
Unlimited Release
Printed January 1999

AUTOMATION, CONTROL AND MODELING OF COMPOUND SEMICONDUCTOR THIN-FILM GROWTH

Michael E. Coltrin, John F. Klem, Hong Q. Hou, W. G. Breiland,
Timothy J. Drummond, Kevin M. Horn, Jeffrey Y. Tsao
Chemical Processing Science Department
Sandia National Laboratories
Albuquerque, NM 87185-0601

ABSTRACT

This report documents the results of a laboratory-directed research and development (LDRD) project on control and agile manufacturing in the critical metalorganic chemical vapor deposition (MOCVD) and molecular beam epitaxy (MBE) materials growth processes essential to high-speed microelectronics and optoelectronic components. This effort is founded on a modular and configurable process automation system that serves as a backbone allowing integration of process-specific models and sensors. We have developed and integrated MOCVD- and MBE- specific models in this system, and demonstrated the effectiveness of sensor-based feedback control in improving the accuracy and reproducibility of semiconductor heterostructures. In addition, within this framework we have constructed "virtual reactor" models for growth processes, with the goal of greatly shortening the epitaxial growth process development cycle.

TABLE OF CONTENTS

AUTOMATION, CONTROL AND MODELING OF COMPOUND SEMICONDUCTOR THIN-FILM GROWTH

I. INTRODUCTION

Despite the sophistication of the two most commonly used compound semiconductor epitaxial growth techniques, molecular beam epitaxy (MBE) and metalorganic chemical vapor deposition (MOCVD), the growth of semiconductor device structures remains something of an art. This is due in part to the poorly characterized thermal and fluid response of typical epitaxial reactors, the complexity of the reactant chemistries, and to the dead-reckoning approach to reactor process control systems which dictates an inflexible time-deterministic specification of the growth process. Typically, the crystal grower, through experience with a particular reactor and chemical system, attains a level of expertise which allows for the inclusion of the effects of reactor dynamic response and reactant chemistry in the growth recipe. However, because this method tends to be more intuitive than quantitative, the production of complicated devices often becomes an expensive and time-consuming iterative process of growth and ex-situ characterization.

The goal of this laboratory-directed research and development (LDRD) project has been to develop a system of monitoring, modeling, and control techniques to both enhance the capabilities of these growth methods, as well as decrease the time, effort, and expense required to grow complex heterostructures within challenging specifications. We have built directly on previous successful work at Sandia in monitoring and modeling. A key point of the program has been the integration of these techniques within a single architecture which has enabled us to increase dramatically process yield and allow use of sophisticated monitoring and control techniques for the growth.

The backbone for achieving these goals is a modular process automation system which may be configured for MOCVD, MBE, and other semiconductor processing tools. The process automation system includes (1) an open, extensible, object-oriented architecture; (2) the capability to interface with newly developed process monitors; (3) a powerful recipe scripting language which allows sensor-driven process control; (4) connectivity to modeling software, thus enabling both model-based control and "virtual reactor" simulation; and (5) statistical process data monitoring capability to enable the analysis of long-term process trends.

This report describes our experimental approach to MOCVD growth and material doping. The in-situ optical reflectance growth monitor, used in both our MOCVD and MBE systems, is discussed next. The next section summarizes our MBE experiments. A simple analytical model of MOCVD growth, which was developed as a "virtual reactor" module, is then discussed. Theoretical models of doping statistics in the AlGaAs system are then described. An overview of the MOCVD reactor automation and control architecture is then given, followed by our thoughts on the future Virtual Reactor architecture.

II. MOCVD GROWTH

Because of their demanding structural, electrical and optical requirements, vertical-cavity surface-emitting lasers (VCSELs) are among the most difficult of optoelectronic devices to grow. For example, the resonant wavelengths associated with their various structural elements -- the top and bottom distributed Bragg reflectors (DBRs), the Fabry-Perot cavity, the quantum wells -- must all overlap within a narrow range for optimum performance. The final lasing wavelength, which represents a convolution of these resonances, will vary in a typical 850-nm VCSEL by 1% (roughly 8.5 nm) for a 1% error in growth rate. Therefore, the accuracy with which growth must be controlled is often better than 0.5%.

To achieve these results, a common configuration is the MOCVD rotating-disk reactor[1] (RDR) fed with trimethylgallium (TMGa), trimethylaluminum (TMAl) and 100% arsine (AsH_3) for AlGaAs growth and disilane (Si_2H_6) and carbon-tetrachloride (CCl_4) for *n*- and *p*-type doping, respectively. Typical growth conditions are described in Figure 1 and in its caption.

Gas source	Bubbler settings and pressures			Flows and pressures			
	Typical total pressure in bubbler (torr)	Typical temperature in bubbler (°C)	Typical vapor pressure in bubbler (torr)	Minimum typical flow in chamber (sccm)	Maximum typical flow in chamber (sccm)	Minimum typical partial pressure in chamber (torr)	Maximum typical partial pressure in chamber (torr)
Viewport purge (H_2 flow)				2.40E+03	2.40E+03	6.10E+00	6.10E+0(
Shroud push (H_2 flow)				1.70E+04	1.70E+04	4.32E+01	4.32E+01
Alkyl push (H_2 plus alkyl flows)				1.20E+03	1.20E+03	3.05E+00	3.05E+0(
Hydride push (H_2 plus hydride flows)				3.00E+03	3.00E+03	7.63E+00	7.63E+0(
$(TMAl)_2$ bubbler (H_2 flow)	700	18	7.90	2.00E+00	9.00E+01		
$(TMAl)_2$ bubbler ($(TMAl)_2$ flow)				2.26E-02	1.02E+00	5.74E-05	2.58E-0:
TMGa bubbler (H_2 flow)	600	-10	39.66	1.00E+00	3.50E+01		
TMGa bubbler (TMGa flow)				6.61E-02	2.31E+00	1.68E-04	5.88E-0:
CCl_4 bubbler (H_2 flow)	600	18	79.20	1.00E-02	2.50E+01		
CCl_4 bubbler (CCl_4 flow)				1.32E-03	3.30E+00	3.36E-06	8.39E-0:
1000 ppm Si_2H_6 in H_2 (total flow)				1.00E-03	5.00E-01		
Si_2H_6 flow				1.00E-06	5.00E-04	2.54E-09	1.27E-0(
100% AsH_3 flow				2.50E+02	2.50E+02	6.36E-01	6.36E-01
Total chamber				2.36E+04	2.36E+04	6.00E+01	6.00E+01

Figure 1: Typical flows and pressures used in our EMCORE model GS3200 RDR for VCSEL growth. A typical rotation rate is 1000 rpm, a typical growth rate is 10 Å/s, and typical substrate temperatures are 630-720°C. Typical substrates are GaAs (100) misoriented 2° toward (110); the slight misorientation improves surface morphology and can help suppress oxygen incorporation in AlGaAs alloys.[2]

The TMGa, TMAl and CCl_4 are modest-vapor-pressure liquids, and so are carried by Pd-cell-purified H_2 into an injection block and then to an inlet flange. The TMGa is typically kept at a bubbler temperature of approximately -10°C, at which temperature its vapor pressure, calculated from[3] $\log_{10}$ p (torr) = 8.495-1824/*T*(K), is approximately 39.66 torr. The TMAl is typically kept at a bubbler temperature of approximately 18°C, at which temperature its vapor pressure, calculated from[4] $\log_{10}$ p (torr) = 7.3147-1534.1/[*T*(K)-53], is approximately 7.9 torr. The CCl_4 is typically kept at a bubbler temperature of approximately 18 °C, at which temperature its vapor pressure, calculated

[1] In our laboratory we use both a commercial EMCORE model GS3200 RDR with a 5" platen as well as home-built research RDRs with 3" platens.

[2] This effect is very pronounced when the miscut is large and towards (111)A -- significantly higher room-temperature photoluminescence (PL) efficiency is observed from $Al_{0.24}Ga_{0.76}As$ quantum wells grown on (311)A than from those grown on (001) substrates.

[3] C. Plass, H. Heinecke, O. Kayser, H. Luth, and P. Balk, J. Crystal Growth **88,** 455 (1988).

[4] Alfa Organometallics for Vapor Phase Epitaxy 1984, Literature Review (Morton Thiokol Inc., Alfa Products, 1984).

from[5] $\log_{10}$ p (torr) = 9375 – 1752.6/T(K), is approximately of 79.2 torr. The total (mostly hydrogen) overpressure within the bubbler, $p_{\text{bubbler total}}$, is typically approximately 600-700 torr, with hydrogen flow rates, F_{Hydrogen}, in the range 2 to 200 sccm. The flow rate of metal alkyl through the bubblers, $F_{\text{metal alkyl}}$, can be calculated[6] to be

$$F_{\text{metal alkyl}} = \varepsilon F_{\text{Hydrogen}} p_{\text{metal alkyl}} / (p_{\text{bubler total}} - p_{\text{metal alkyl}}) \quad (1)$$

where $p_{\text{metal alkyl}}$ is the saturated vapor pressure of the metal alkyl. At typical overpressures, the efficiency of the bubbler, ε, can be assumed to be unity to within a few percent,[7] though it is possible, especially at lower overpressures, for the efficiency to be significantly less than unity. In these situations, the efficiency of the bubbler is a complicated function of $p_{\text{metal alkyl}}$, $p_{\text{bubbler total}}$, the amount of liquid left in the bubbler, and the specific configuration and size of the bubbler.

The flow of gas through the reactor is typically dominated by H_2, approximately 23.6 slm, and includes the total (H_2 push plus arsine) flow associated with the arsine (3 slm), the total (H_2 push plus metal alkyl plus dopant) flows associated with the metal alkyl bubblers and dopants (1.2 slm), various purge (e.g., viewport) flows (2.4 slm), a very small push flow for the n-type dopant Si_2H_6 (from a pressurized gas bottle of 1000 ppm Si_2H_6 in pure H_2), and the balance (17 slm) for a shroud flow. The total reactor pressure is typically 60 Torr, with the AsH_3 flow rate, the growth rate, and V/III ratio fixed at 250 sccm, 10 Å/s, and ~125, respectively, throughout a growth run. The wafer temperature is typically 720°C as measured by a thermocouple calibrated by the melting points of eutectic alloys. However, a lower growth temperature (630°C) is sometimes used for the cap-layer growth to achieve a higher p-type doping concentration, and a slower etchback rate. The substrate is typically rotated at 1000 rpm.

The growth parameters for a set of representative layers in a typical 850-nm VCSEL are listed in the spreadsheet in Figure 2. The spreadsheet contains the detailed flow rates for the H_2 carrier gas through the TMGa, TMAl and carbon tetrachloride bubblers. The resulting TMGa, TMAl, disilane and carbon tetrachloride flow rates can be calculated from Equation 1, and the partial pressures of the reactants can be calculated using a simple ideal-gas dilution equation:

$$p_i = (F_i / F_{\text{reactor total}}) p_{\text{reactor total}}, \quad (2)$$

where p_i and F_i are the partial pressures and flows of component i.

The relationships between the metal alkyl partial pressures and the growth rates are typically linear, as illustrated on the left side of Figure 3. Therefore, the growth rates can be expressed as $g_o = A_1 p_{\text{TMGa}} + A_2 p_{\text{TMAl}}$. Note that a complicating aspect of growth is the

---

[5] DIPPR Data Compilation of Pure Compound Properties, Design Institute for Physical Properties Data, American Institute of Chemical Engineers, 1987.

[6] S.D. Hersee and J.M. Ballingall, "The Operation of Metalorganic Bubblers at Reduced Pressure," J. Vac. Sci. Technol. **A8**, 800 (1990).

[7] K.C. Baucom, K.P. Killeen and H.K. Moffat, "Monitoring of MOCVD Reactants by UV Absorption", J. Electronic Materials **24**, 1703 (1995).

presence of a simultaneous etching reaction associated with the carbon tetrachloride precursor. As also shown in Figure 3, that reaction is also linear with the carbon tetrachloride partial pressure, so one can typically subtract the etch rate from the growth rate in the absence of carbon tetrachloride to get the actual doped-layer growth rate.

Material	Al/Ga start ratio	Al/Ga end ratio	Thickness Å	Growth rate Å/s	Growth rate with etchback Å/s	Time min	Carrier type	Carrier concentration cm^{-3}	Substrate temperature °C	TMG1 total flow sccm	TMA1 (start) total flow sccm	CCl_4 total flow sccm	Si_2H_6 total flow sccm	Loops
AlGaAs	0.16		363.8	10.00	9.555	0.635	p	1.0E+18	720	24.7	11.1	1.28		1
AlGaAs	0.20	0.16	39.5	10.00	9.727	0.068	p	1.0E+18	720	23.6	14.0	0.80		1
AlGaAs	0.34	0.20	45.2	10.00	9.920	0.076	p	1.0E+18	720	19.5	25.0	0.27		1
AlGaAs	0.54	0.34	40.0	10.00	9.962	0.067	p	1.0E+18	720	13.6	41.4	0.20		1
AlGaAs	0.74	0.54	41.6	10.00	9.983	0.069	p	1.0E+18	720	7.7	58.0	0.20		1
AlGaAs	0.88	0.74	50.0	10.00	9.992	0.083	p	1.0E+18	720	3.5	69.2	0.20		1
AlGaAs	0.92	0.88	45.3	10.00	9.994	0.076	p	1.0E+18	720	2.3	72.3	0.20		1
AlGaAs	0.92		1182.0	10.00	9.994	1.971	p	1.0E+18	720	2.3	72.3	0.20		1
AlGaAs	0.98	0.92	40.0	10.00	9.996	0.067	p	1.0E+18	720	0.6	76.8	0.20		1
AlGaAs	0.98		80.0	10.00	9.996	0.133	p	1.0E+18	720	0.6	76.8	0.20		1
AlGaAs	0.92	0.98	40.0	10.00	9.994	0.067	p	1.0E+18	720	2.3	72.3	0.20		1
AlGaAs	0.92		481.0	10.00	9.994	0.802	p	1.0E+18	720	2.3	72.3	0.20		1
AlGaAs	0.88	0.92	45.3	10.00	9.992	0.076	p	1.0E+18	720	3.5	69.2	0.20		1
AlGaAs	0.74	0.88	50.0	10.00	9.983	0.083	p	1.0E+18	720	7.7	58.0	0.20		1
AlGaAs	0.54	0.74	41.6	10.00	9.962	0.070	p	1.0E+18	720	13.6	41.4	0.20		1
AlGaAs	0.50	0.54	39.2	10.00	9.956	0.066	p	1.0E+18	720	14.7	38.1	0.20		1
AlGaAs	0.50		25.0	10.00	9.956	0.042	p	1.0E+18	720	14.7	38.1	0.20	]	1
pause					0.000	0.050			720					
AlGaAs	0.20		238.0	10.00	9.727	0.408	p	1.0E+18	720	23.6	14.0	0.80		
AlGaAs	0.20		194.0	10.00	9.781	0.331	p	8.0E+17	720	23.6	14.0	0.64		
AlGaAs	0.20		148.5	10.00	9.862	0.251	p	5.0E+17	720	23.6	14.0	0.41		
AlGaAs	0.20		200.0	10.00	10.000	0.333			720	23.6	14.0			
GaAs			80.0	8.00	8.000	0.167			720	23.6			[	5
AlGaAs	0.20		80.0	10.00	10.000	0.133			720	23.6	14.0		]	5
AlGaAs	0.20		120.0	10.00	10.000	0.200			720	23.6	14.0			
AlGaAs	0.20		148.5	10.00	10.000	0.248	n	5.0E+17	720	23.6	14.0		0.08	
AlGaAs	0.20		194.0	10.00	10.000	0.323	n	8.0E+17	720	23.6	14.0		0.13	
AlGaAs	0.20		238.0	10.00	10.000	0.397	n	1.0E+18	720	23.6	14.0		0.17	
AlGaAs	0.60		67.0	10.00	10.000	0.112	n	1.0E+18	720	11.8	46.4		0.17	[1
AlGaAs	0.74	0.60	41.6	10.00	10.000	0.069	n	1.0E+18	720	7.7	58.0		0.17	1
AlGaAs	0.88	0.74	50.0	10.00	10.000	0.083	n	1.0E+18	720	3.5	69.2		0.17	1
AlGaAs	0.92	0.88	45.3	10.00	10.000	0.076	n	1.0E+18	720	2.3	72.3		0.17	1
AlGaAs	0.92		481.0	10.00	10.000	0.802	n	1.0E+18	720	2.3	72.3		0.17	1
AlGaAs	0.98	0.92	40.0	10.00	10.000	0.067	n	1.0E+18	720	0.6	76.8		0.17	1
AlGaAs	0.98		80.0	10.00	10.000	0.133	n	1.0E+18	720	0.6	76.8		0.17	1
AlGaAs	0.92	0.98	40.0	10.00	10.000	0.067	n	1.0E+18	720	2.3	72.3		0.17	1
AlGaAs	0.92		1182.0	10.00	10.000	1.970	n	1.0E+18	720	2.3	72.3		0.17	1
AlGaAs	0.88	0.92	45.3	10.00	10.000	0.076	n	1.0E+18	720	3.5	69.2		0.17	1
AlGaAs	0.74	0.88	50.0	10.00	10.000	0.083	n	1.0E+18	720	7.7	58.0		0.17	1
AlGaAs	0.60	0.74	56.2	10.00	10.000	0.094	n	1.0E+18	720	11.8	46.4		0.17	1
pause						0.060			720					1
AlGaAs	0.16		107.4	10.00	10.000	0.179	n	1.0E+18	720	24.7	11.1		0.17	1
AlGaAs	0.16		363.8	10.00	10.000	0.606	n	1.0E+18	720	24.7	11.1		0.17	] 1

Figure 2: A spreadsheet containing the flow rates and other parameters associated with the various hydrogen carrier, organometallic and hydride precursors during growth of representative layers within an 850-nm VCSEL heterostructure. The overall growth conditions are the same as those listed in Figure 1.

An additional complication is that, though the growth rates are independent of the composition of the growing material, the etch rate is not. As indicated on the right side of Figure 3, the etch rate depends strongly on the composition, varying approximately as $1 - (1+e^{(0.541-xAlAs)/0.158})^{-1}$. In other words, the etch rate decreases sharply for increasing Al content in the alloy, and is very selective towards GaAs over AlAs. The overall growth rate can thus be expressed as:

$$g = A_1 p_{TMGa} + A_2 p_{TMAl} - A_3 \left[1 - \left(1 + e^{(0.541 - xAlAs/0.158)}\right)^{-1}\right] \qquad (3)$$

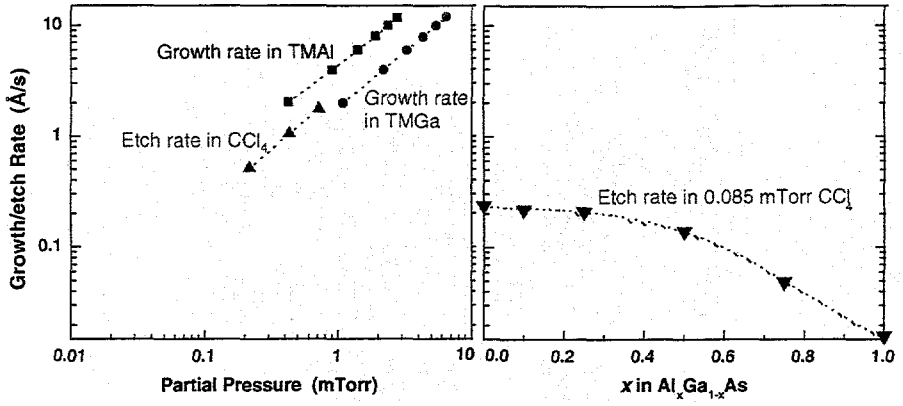

Figure 3: Growth rates as functions of partial pressure for GaAs from TMGa and AlAs from TMAl (left), and etch rates as functions of partial pressure and composition for GaAs and AlGaAs etching by CCl_4 (left and right). The temperature for all of the data was 720°C, and the CCl_4 partial pressure for the right side of the Figure was 0.085 mTorr. The data were collected using optical reflectance measurements similar to those described in the next section.

Typical values for the A_1, A_2 and A_3 factors for the conditions used in Figures 1 and 2 are $A_1 \cong 1.8$ Å/(s-mTorr), $A_2 \cong 4.5$ Å/(s-mTorr), and $A_3 \cong 2.6$ Å/(s-mTorr). Note that, though this equation could be applied at temperatures and flow conditions other than that for which we have shown data, for other temperatures and flow conditions (total pressures, spin rates, etc.) the A_1, A_2 and A_3 factors will all vary in a complex way.

III. DOPING EXPERIMENTS

To create active optoelectronic devices, it is also necessary to dope the materials. Doping represents at most a very minor perturbation to the fluid dynamics and chemistry (even for VCSEL structures, where it is necessary to dope to relatively high levels). However, it is of major importance in determining the electronic properties of the final device structure.

For the n-type dopants, the group-IV element Si has been the most commonly used, due to its combination of low diffusivity and low elemental vapor pressure. In addition, when incorporated from a disilane source, the incorporation efficiency is extremely high and the incorporation rate tends to be limited by mass transport rather than by surface kinetics. As a consequence, as illustrated in Figure 4, doping levels increase linearly with increasing disilane (Si_2H_6) partial pressure, with very little temperature dependence[8] for sufficiently high total pressures.[9] At a temperature of 630°C, this dependence can be written as

$$n = A_4 p_{Si_2H_6}, \tag{4}$$

where $A_4 \cong 2.7\times10^{21}$ mTorr^{-1}cm^{-3} is a calibration factor similar to the A_1, A_2 and A_3 factors discussed in Section II.

---

[8] T.F. Kuech, E. Veuhoff and B.S. Meyerson, "Silicon doping of GaAs and AlxGa1-xAs using disilane in metalorganic chemical vapor deposition," J. Crystal Growth **68**, 48 (1984).

[9] H.K. Moffat, T.F. Kuech, K.F. Jensen, P.J. Wang, "Gas-phase and surface reactions in Si Doping of GaAs by Silanes," J. Crystal Growth **93**, 594 (1988).

Intentionally Left Blank

For the p-type dopants, the group-IV element C has become increasingly attractive and commonly used, again due to its combination of low diffusivity and low elemental vapor pressure. However, when incorporated from a carbon tetrachloride source, the incorporation efficiency is not very high and the incorporation rate tends to be limited by surface kinetics rather than by mass transport. As a consequence, as shown in Figure 4, doping levels increase linearly with increasing carbon tetrachloride partial pressure, with a fairly strong temperature dependence. At a temperature of 630°C, this dependence can be written as

$$p = A_5 p_{CCl_4}, \tag{5}$$

where $A_5 \cong 1.2\times10^{19}$ mTorr^{-1}cm^{-3}, like A_4, is an additional calibration factor.

In this sense, these two dopants, Si from disilane and C from carbon tetrachloride, represent two extremes of behavior: one mass-transport-limited and the other surface-kinetic-limited.

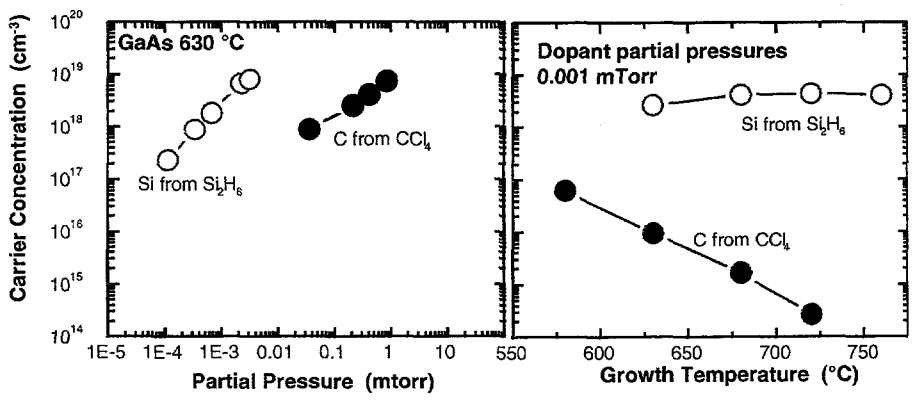

Figure 4: Carrier concentrations versus partial pressure (at 630°C) and versus temperature (scaled to correspond to 0.001 mTorr partial pressures) for n-type doping from disilane and p-type doping from carbon tetrachloride.

Intentionally Left Blank

IV. IN SITU OPTICAL REFLECTANCE GROWTH MONITOR

Having established semi-empirical relations between growth rates and the various partial pressures (or flows) such as that given by Equation 3, it is necessary to calibrate the A_1, A_2 and A_3 factors as accurately (within 1%) as possible. This is especially critical for VCSEL growth, for which even very slight day-to-day drifts in machine operating response (and hence the A_1, A_2 and A_3 factors) lead to drifts in growth rate, composition and doping which are detrimental to performance.

Recently, a new generation of *in situ* optical measurement techniques based on optical (both normal and off-normal incidence) reflectance have been developed. The normal-incidence technique has become especially valuable for day-to-day or week-to-week calibrations because of its robustness and accuracy. By using a combination of *in situ* normal-incidence reflectance and a well-understood functional relationship between source gas flow rates and growth rate behavior such as that given in Equation 3, a single one-hour run can be used to calibrate the growth conditions required for an entire VCSEL structure as well as for a wide range of other device structures based on AlGaAs/GaAs materials. In this section, we discuss the practical application of this technique for reactor calibration and real-time growth monitoring.

The technique as currently used employs two simple concepts. The first concept is that, as a thin film grows, the normal-incidence reflectance of monochromatic light undergoes oscillations whose frequency is proportional to the product of the refractive index and the growth rate. These oscillations may be used to extract the growth rate of the semiconductor film. It is straightforward to extend this concept and to model the reflectance from a smooth semiconductor substrate with an arbitrary number of smooth, homogeneous films deposited on it. The only parameters required are the complex refractive index for the substrate and the thickness and refractive index of each layer. Such a model could, in principle, be used to extract the growth rate from the topmost film. Unfortunately, this approach becomes impractical for a multiple-layer film because errors in underlying film parameters propagate amplitude and phase deviations that become unacceptably large for the topmost film as the growth proceeds.

The second concept is that this multiple-layer reflectance modeling problem can be simplified enormously through the use of so-called virtual interface methods.[10] One chooses a virtual interface position that lies anywhere within the topmost film. It is then possible to rigorously describe the effects of all underlying layers as a single effective complex refractive index, N_{vs}, of an effective virtual substrate. The precise value of N_{vs} can, in principle, only be calculated from a complete knowledge of all the refractive indices and thicknesses of the underlying layers. However, if N_{vs} is taken to be an unknown, it is always true that any multiple-layer structure requires only two parameters, the real and imaginary parts of N_{vs}, to describe the effects of all underlying layers below the virtual interface boundary.

---

[10] D. E. Aspnes, J. Opt. Soc. Am. **A10**, 974 (1993).

Intentionally Left Blank

Analysis of the topmost layer is thus made completely independent of the optical constants and interface positions of underlying layers. By choosing a new virtual interface position with each new layer, cumulative effects are eliminated in the analysis of a growing multiple-layer film structure.[11]

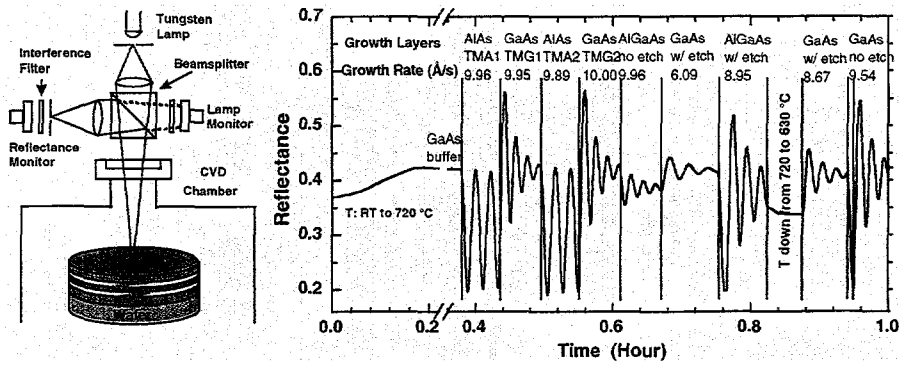

Figure 5: Schematic of apparatus (left) used to measure absolute optical reflectances (right) during growth runs specially designed to calibrate the machine response given by Equation 3.

In our research, the virtual interface method was first used to establish the relationship between source gas flow rates and semiconductor growth. For example, Equation 3 was based on extensive studies showing that the growth rates of GaAs and AlAs are linear in source gas flow rate (as illustrated in Figure 3) and that growth of alloys of $Al_xGa_{1-x}As$ is to a very high degree of accuracy a linear combination of growth from the individual Ga and Al source gases. It was also based on studies of etching during doping as a function of $Al_xGa_{1-x}As$ composition (as illustrated in Figure 3) and temperature.

Having established accurate relationships between source gas flow rates and semiconductor growth, it is possible to devise compact runs, such as that illustrated in Figure 5, to calibrate growth (essentially the A_1, A_2 and A_3 factors of Equation 3).[12,13] A 7-watt W-halogen lamp was used as the light source and a silicon photodiode with a 10-nm-bandwidth interference filter at 550 nm was used to detect the reflectance signal. The whole assembly was mounted directly on the top miniflange window of the reactor. The growth rates achieved by using various alkyl sources were determined from fitting the reflectance waveform with the virtual interface model. The reduction of the growth rate due to the etchback effect of AlGaAs and GaAs by CCl_4 with different C doping levels at different temperatures is also extracted from this calibration run. All together, six layers are required to calibrate two Al sources, two Ga sources, and the CCl_4 etchback rates at 720 °C and 630 °C.

[11] W.G. Breiland and K.P. Killeen, "A virtual interface method for extracting growth rates and high temperature optical constants from thin semiconductor films using in situ normal incidence reflectance," J. Appl. Phys. **78**, 6726 (1995).

[12] H.Q. Hou, W.G. Breiland, B.E. Hammons, and H.C. Chui, "In situ growth rate measurements by normal-incidence reflectance during MOVPE growth," Electrochemical Soc. Proc. **96-2**, 27 (1996).

[13] W.G. Breiland H.Q. Hou, H.C. Chui, and B.E. Hammons, "In situ pre-growth calibration using reflectance as control strategy for MOCVD fabrications of device structures," J. Crystal Growth **174**, 564 (1997).

Intentionally Left Blank

V. MOLECULAR BEAM EPITAXY

In contrast to MOCVD, many aspects of molecular beam epitaxial (MBE) growth of common materials can be understood with little concern for the underlying chemistry. In the usual growth regimes of mixed-group-III III-V compounds, steady-state material compositions are determined simply by the relative arrival rates of the corresponding group-III materials. A handicap of MBE relative to MOCVD, however, is the instability of these reactant fluxes over periods of hours or longer. This is due to fundamental design features of MBE reactant sources, or effusion cells. For certain types of device structures, these instabilities are serious enough that even routine pre-growth calibrations, such as flux measurement by reflection high-energy electron diffraction oscillation measurements, are not sufficient to insure the desired growth accuracy.

In this work, we have employed in-situ optical reflectance to monitor material growth during the fabrication of a device structure that has performance characteristics strongly dependent on layer thicknesses. The optical reflectance signal is processed to provide growth rate data throughout the run, and is employed in a feedback algorithm to modify the target device structure during growth to achieve the desired device performance, regardless of the deviations in material growth rate.

This type of feedback control is novel in that it does not correct deviations in the performance of the epitaxy system by direct control of a process variable (such as an effusion cell flux), but rather achieves control over a resulting device parameter by subtly changing the device epitaxial structure to be grown in response to inaccuracies in the growth of earlier portions of the structure. This type of feedback control is necessarily somewhat structure-specific, but we have shown that it is general enough that small changes in the feedback algorithm can accommodate significant changes in the nominal design of the structure. The reasons for choosing this type of control over direct process variable control are that it functions well in the presence of process monitor noise (i.e., has a long integration time), and for the type of structure we used it can implement the feedback as a one-time correction. Because of this feature, the feedback control can contain computation-intensive models, or even utilize (slow) human input as part of the algorithm.

The target device is an optical reflectance modulator designed to operate at a wavelength of 1.320 μm. This device structure consists of a resonant optical cavity formed by two semiconductor dielectric mirrors with a semiconductor quantum well active region between them. The device parameter most difficult to control in this structure is the optical wavelength at which the cavity is resonant. This resonance wavelength is a function of the refractive indices and thicknesses of both the mirror materials and the active region. For satisfactory device performance, the resonance wavelength at the center of the wafer must be within 1.322-1.330 μm, a range of 0.6%. In previous attempts at the growth of this structure by MBE, it was found that the yield of wafers grown to the nominal specification before the application of feedback control was less than 50% due to this constraint alone.

A conventional approach was used for modeling the MBE effusion cell flux vs. temperature relationship. A static model was used, with

$$F = Ae^{-B/T}, \tag{6}$$

where F is the atomic flux from the effusion cell, T is the temperature in K, and A and B are experimentally determined parameters. We have observed that the primary uncertainty in this model is the parameter A, which is subject to substantial variation on a time scale of hours due to depletion of source material, while parameter B is primarily a function of effusion cell construction and type of source material being used. The point of using feedback control is therefore to compensate for measurement error and drifts in the parameter A.

The in-situ reflectance monitor was used to provide real-time measurement of the growth rate of the individual quarter-wavelength layers composing the first part of the first mirror in the device structure. Based on the measured growth rates and nominal growth times, a model of the actual (versus nominal) device structure was constructed. The wavelength of the cavity resonance is calculated from structure models using a conventional matrix approach. Because only data collected during the first part of the growth is available, an essential component of the algorithm is a method of predicting, based on the available data, what layer thicknesses will be grown for the remainder of the structure if no feedback control is applied. Two different predictors were compared for arriving at thicknesses for the remaining mirror layers. Based on comparisons of the model predictions with subsequent ex-situ measurements, the best was selected. This predictor was quite simple: the growth rate for all unmeasured mirror layers was estimated to be the average of the growth rate of the five most recently measured layers. For the growth rate of the active region, the nominal growth rate was assumed, since resonance wavelength errors were calculated to be a factor of 4 less sensitive to cavity thickness errors than mirror thickness errors for the structure under consideration.

Subsequent application of this predictor showed that in cases where the growth rates departed substantially from nominal, the cavity resonance wavelength could fall outside the target wavelength range. Much of this error was seen to result from the cavity thickness error which remained uncompensated. To estimate the growth rate for the cavity, a second predictor was developed. Inputs to this predictor were the average growth rates measured during the run for both the high- and low-index layers of the mirror. The output of the predictor was the average growth rate for the cavity materials, and was calculated as

$$C = DG_H + EG_L, \tag{7}$$

where G_H and G_L were the growth rates of the high- and low-index materials, respectively, and D and E were coefficients determined by a least-squares minimization of the predicted resonance wavelength error for a number of growths. This predictor implicitly assumes that the growth rate errors are related to errors in the estimation of the effusion cell A parameter. In addition, it should be mentioned that the accuracy of the

estimator will be limited by the fact that it has only two inputs (G_H and G_L), which cannot be fully correlated with the three sources of error (parameters A for the three effusion cells used for active region and mirror growth). Even with these limitations, the cavity growth rate estimator was shown to significantly improve the resonance position prediction accuracy of the model, particularly when the measured growth rates departed more than 1% from the nominal values.

The feedback algorithm began with constructing a model of the structure being grown, including predicted thicknesses for the active region and later mirror portions. The resonance wavelength for this model structure was then calculated, and based on the deviation of the predicted and desired resonance wavelengths, a scaling factor was calculated for the remaining mirror layers. The effect of this scaling factor is to compensate for the previous inaccurately grown mirror layers, and the yet-to-be inaccurately grown cavity. This scaling factor was empirically determined, and is of course specific to the nominal structure grown, but otherwise only a simple function of the predicted resonance wavelength errors, and therefore insensitive to the details of exact sequence of layer thicknesses which produced that error. Once calculated, this scaling factor was applied as a programmed input to the growth recipe.

The feedback control algorithm described above, but without cavity growth rate prediction, was applied to a series of reflectance modulator structure growths. With feedback, the cavity resonance position was controlled with a standard deviation of approximately 0.2%, and only 1 out of 8 growths produced structures with resonance positions outside the 1.322-1.330 window. Based on the in-situ data, it was clear that 3 of these structures would not have met the resonance position specification without feedback control. Subsequent growths which included cavity growth rate prediction have had even better control over the resonance position.

Extension of this control algorithm to modified structures has also been demonstrated. A digitally-graded mirror version of the modulator structure was grown using essentially the same algorithm. The required modifications to the algorithm were further estimation of the thicknesses of some very thin portions of the new structure for which direct growth rate measurements were not possible, and simple changes to the structure model corresponding to the changes in the nominal structure. It was found that no changes in any of the adjustable model parameters were otherwise necessary to retain excellent prediction and control. Changes to the nominal structure including doubling the cavity thickness and changing the number of mirror periods were accomplished in the same way, with no significant loss in control accuracy.

In summary, we have demonstrated a simple set of MBE reactor, epitaxial structure, and in-situ sensor models which are capable of providing precise control of a critical device parameter using an epitaxial growth feedback control algorithm. The technique is somewhat structure-specific, but is flexible enough to be adaptable to a wide range of structures within the general category of vertical resonant-cavity devices. This technique has significantly improved our ability to grow a challenging epitaxial structure within

specification, and provides a model for application to a wider range of epitaxial growth control issues.

VI. MOCVD GROWTH MODEL

In the following, we present a simple, analytical treatment of transport in an RDR MOCVD reactor with special emphasis on transport across the boundary layer, and derive semi-quantitative expressions for growth rates and composition as a function of reactor conditions such as total pressure, flow rates, reactant partial pressures, and disk-rotation rate. These expressions enable growth rates and reactor operation in the AlGaAs system to be calculated to within factors of two or better, using only simple scaling relationships.

Much of the simplicity derives from the well-behaved and understood fluid flow in the RDR, as approximated by the ideal, infinite-radius, one-dimensional analysis. These approximations are usually valid for the conditions under which deposition is usually performed. For typical AlGaAs OMVPE, the situation is made even simpler in that growth is nearly mass-transport limited in the group-III species. Therefore, the composition of alloys with mixed group-III species can typically be linearly interpolated from the growth rates due to the individual group-III species.

The fluid is assumed to be composed of H_2 in great excess, with trace quantities of the group-III precursor. Thus, the transport properties of the fluid are well described by those of H_2 alone. We also assume the following baseline conditions: 60 Torr total pressure, 1000 rpm rotation rate, 720°C disk temperature, and H_2 carrier gas.

For an isothermal disk and fluid, the dimensionless axial velocity far from the disk is H_∞ = -0.8838. The natural "drawing velocity" of the disk is, in dimensional units (cm/s),

$$u_\infty = H_\infty \sqrt{\omega \nu_\infty} = -0.8838 \sqrt{\omega \nu_\infty}. \tag{8}$$

The kinematic viscosity scales with temperature and pressure approximately as

$$\nu = \nu_{\text{ref}} \left(p_{\text{ref}} / p \right) \left(T / T_{\text{ref}} \right)^{1.7}, \tag{9}$$

where ν_{ref} is the kinematic viscosity at a specified reference pressure p_{ref} and temperature T_{ref}, and $\nu_{\text{ref}} = \mu_{\text{ref}} / \rho_{\text{ref}}$. It is convenient here to choose the reference pressure and temperature to be 760 Torr and 300 K, at which the kinematic viscosity of H_2 is ν_{ref} = 1.09 cm^2/s, evaluated using the Chemkin transport library.[14]

[14] R.J. Kee, G. Dixon-Lewis, J. Warnatz, M.E. Coltrin, and J.A. Miller, "A Fortran Computer Code Package for the Evaluation of Gas-Phase Multicomponent Transport Properties," Sandia National Laboratories Report, **SAND86-8246** (1986).

The flow rate Q (in sccm) required to match the natural disk "drawing rate" for a reaction chamber of radius r_c (in cm) is

$$Q = u_\infty 60\pi r_c^2 \left({}^{p}\!/\!_{760\,\mathrm{torr}} \right) \left({}^{273.15\,\mathrm{K}}\!/\!_{T_\infty} \right). \tag{10}$$

For 60 Torr, u_∞ = 33.7 cm/s[15], which (for a cell radius of 5.72 cm) gives the flow rate required to match the pumping action of the disk as Q = 14.9 slm. We note that the natural drawing velocity (and thus volume flow rate) depends upon the disk temperature in the non-isothermal case, but only very weakly;[16] thus, for the purpose of this analysis, we neglect the disk-temperature dependence of the fluid flow.

The momentum boundary layer thickness can be defined as the distance at which the (dimensionless) radial and circumferential velocity components, F and G, respectively, drop to nearly zero (i.e., are less than some arbitrary small value, such as 0.01). For the isothermal case this occurs at a dimensionless height of about $\eta = 5$. In dimensional units (cm) the momentum boundary layer thickness is thus

$$\delta_v = 5\sqrt{{}^{\nu_\infty}\!/\!_{\omega}}. \tag{11}$$

The thermal and concentration boundary layer thicknesses δ_T and δ_c, respectively, are related to δ_v through the Prandtl (Pr) and Schmidt (Sc) numbers as

$$\delta_T = {}^{\delta_v}\!/\!_{\sqrt{\mathrm{Pr}}} \tag{12}$$

$$\delta_c = {}^{\delta_v}\!/\!_{\sqrt{\mathrm{Sc}}}. \tag{13}$$

The Prandtl and Schmidt numbers are defined as

$$\mathrm{Pr} = {}^{\nu_\infty c_{p\infty}}\!/\!_{k_\infty} \tag{14}$$

$$\mathrm{Sc} = {}^{\nu_\infty}\!/\!_{D_\infty}, \tag{15}$$

where μ_∞, $c_{p\infty}$, k_∞ and D_∞ are the mixture viscosity, specific heat, thermal conductivity, and reactant diffusivity (taken to be that of the group-III precursor), respectively, evaluated at the inlet.

---

[15] This value, calculated using Equation 8, is slightly less than the 34.0 cm/s calculated using SPIN; the variance is due to slight differences in the calculation of the kinematic viscosity.

[16] The difference in ideal flow velocity between a 300 and 1000 K disk temperature is 11%, i.e., 34.0 vs 30.2 cm/s, respectively.

The relevant transport properties can all be evaluated straightforwardly from simple scaling relationships. The viscosity can be evaluated from Equation 9. The specific heat $c_{p\infty}$ is approximately independent of temperature and pressure, with a reference value for H_2 of $c_{p\infty} = 1.43\text{x}10^8$ erg/(gK). The thermal conductivity is independent of pressure, and scales with temperature as

$$k = k_{\text{ref}}\left(T/T_{\text{ref}}\right)^{0.7}, \tag{16}$$

where the reference value for H_2 at $T_{\text{ref}} = 300$ K is $k_{\text{ref}} = 1.87\text{x}10^4$ erg/(cmKs). The diffusion coefficient scales approximately as

$$D = D_{\text{ref}}\left(p_{\text{ref}}/p\right)\left(T/T_{\text{ref}}\right)^{1.7}, \tag{17}$$

where, at $T_{\text{ref}} = 300$ K and $p_{\text{ref}} = 760$ Torr, $D_{\text{ref}} = 0.39$ and 0.40 cm^2/s for TMGa and TMAl, respectively.

For the baseline case, the momentum boundary layer thickness is $\delta_v = 1.8$ cm. The Prandtl and Schmidt numbers are Pr = 0.69 and Sc = 2.81 for these conditions. Thus, the thermal boundary layer thickness is $\delta_T = 2.2$ cm, and the concentration boundary layer thickness is $\delta_c = 1.0$ cm, for TMGa as the group-III precursor.

The details of the gas-phase and surface reaction kinetics in AlGaAs growth are quite complicated. However, if the goal is merely to calculate growth rates and film compositions for this system, a very simple chemistry model can be employed. Under normal growth conditions, deposition is limited by transport of the group-III element to the surface. Although gas-phase reactions of the precursors do occur, the diffusion coefficients, and thus the transport to the surface, of the group-III fragments (for example TMGa, DMGa, MMGa) are similar. Therefore, we will neglect gas-phase reactions in this treatment, and just worry about the net flux of the group-III element to the surface as carried by the precursor molecule.

It is then a reasonable approximation, consistent with this analytical treatment, to assume that the dimensionless reaction probability or sticking coefficient (γ) for the group-III precursor at the growth surface, is unity. More detailed comparisons with experiment, show that such a unit sticking coefficient over predicts the growth rate, but not by more than 50%, which is within the desired level of fidelity of our simple analysis. The model below could be used with $\gamma < 1$ (and its value determined by experiment), with no modification in the theory required. A more complicated treatment of the chemistry would involve simultaneous flux-matching boundary conditions (for the group-V species), and possibly several heterogeneous reactions.

The sticking probability γ can be converted to a first-order (heterogeneous) reaction rate constant k_r (in cm/s) as

$$k_r = 3638\gamma\sqrt{T/W_{\text{precursor}}}, \tag{18}$$

where $W_{precursor}$ (in g/mol) is the group-III precursor molecular weight. At a reference temperature of T_{ref} = 300 K and for a unit sticking probability γ= 1, the reaction rate constants are k_r = 10,260 and 12,950 cm/s for TMGa and TMAl, respectively.

The boundary condition on the gas-phase group-III precursor states that the flux to the surface matches the rate of destruction due to heterogeneous reaction, i.e.,

$$D\left[dX/dZ\right]_{z=0} = k_r X_o \tag{19}$$

where D is the group-III diffusion coefficient, X is the group-III mole fraction, and X_o is the group-III mole fraction at the surface. If we assume a linear drop in the concentration across the boundary layer (from the inlet value to the concentration at the growth surface), the boundary condition becomes

$$D(X_\infty - X_o)/\delta_c = k_r X_o \ . \tag{20}$$

Or, rearranging,

$$X_o/X_\infty = 1/[1+Da], \tag{21}$$

where Da is the surface Damköhler number, $Da = \delta_c k_r/D$.

Because the diffusion coefficient is temperature dependent, its value is calculated at the temperature mid-way through the concentration boundary layer. (We also assume a linear temperature gradient between T_o at the surface and T_∞ at $z = \delta_T$. Thus, the temperature at $\delta_c/2$ differs somewhat from the average of T_o and T_∞.) For our baseline conditions, the diffusion coefficients for TMGa and TMAl at $\delta_c/2$ are 27.4 and 27.8 cm^2/s, respectively, and the Damköhler numbers are 425 and 530, respectively. When $Da >> 1$, the system is transport-limited, i.e., chemical destruction of the precursor is fast relative to the ability to transport the reactant to the surface.

From this analysis, we can now calculate the growth rate once the inlet mole fraction is specified. The growth rate (in cm/s) is

$$G = \left(W_{solid}/\rho\right) k_r X_o c, \tag{22}$$

where W_{solid} is the molecular weight (W_{solid} = 144.6 g/mole for GaAs or W_{solid} = 109.8 g/mole for AlAs), ρ is the solid density (5.32 g/cm^3 for GaAs or 3.73 g/cm^3 for AlAs), and c is the total (z-independent) concentration of species (in moles/cm^3), which obeys the ideal-gas-law scaling relation

$$c = c_{ref}\left(p_{ref}/p\right)\left(T/T_{ref}\right), \tag{23}$$

where c_{ref} = (1 mole) / (22,400 cm^3) at p_{ref} = 760 torr and T_{ref} = 273.15 K.

We can compare this simple model both to the numerically exact results from the SPIN computer program and from experiment. For TMGa precursor we take the case of $X_\infty = 1.3 \times 10^{-4}$, and for TMAl we take the case of $X_\infty = 1.5 \times 10^{-4}$. For these comparisons, we have used 70 Torr total pressure and 640°C, conditions that correspond to experiments mentioned later, but not the baseline conditions discussed in Section II. The simple model calculates the precursor mole fractions at the surface to be $X_o = 2.6 \times 10^{-7}$ and 2.4×10^{-7}, respectively, compared with the results from SPIN of 3.0×10^{-7} and 2.7×10^{-7}, respectively. The simple model calculates the growth rate for GaAs from TMGa under these conditions as 9.1 Å/s, compared to 10.2 Å/s calculated by SPIN, and an experimental value of 6.2 Å/s. For growth of AlAs from TMAl, the model calculates a growth rate of 10.3 Å/s vs. 11.7 Å/s from SPIN, and an experimental value of 7.0 Å/s.

This simple model agrees with the rigorous treatment in SPIN to within about 10%, indicating the scaling laws and simple treatment of the fluid flow and transport are sufficiently accurate. The model over predicts the growth rates by roughly 50% compared to experiment, which is directly attributable to the assumption of a unit sticking coefficient. Using a sticking coefficient (or rate constant) derived from growth rate measurements could, of course, be used to "calibrate" the model if desired, for more quantitative applications.

The model over-predicts growth of GaAs and AlAs by almost exactly the same linear scaling factor. Growth rates in the AlGaAs alloy system are found to be simply additive, i.e., the AlGaAs growth rate is just the sum of the growth rates from GaAs and AlAs when either group-III precursor is used alone, and the alloy composition is determined simply by the ratio of the molar production rates. Thus, our simple model is expected to be quite accurate in calculating alloy composition.

One strength of this model comes from the understanding of scaling relationships that it provides. It is apparent from the formulas that the boundary layer thicknesses all scale as $\omega^{-1/2}$ and $p^{-1/2}$, and thus the growth rate scales with $\omega^{1/2}$ and $p^{1/2}$, and (for fixed mole fractions of the reactant gases) the growth rate varies approximately as $T_o^{1/2}$. This temperature dependence is not due to the square root dependence of the rate constant k_r, as might be supposed. The rate constant drops out of the final calculation of growth rate, as it should if the system is transport limited. Instead, the final growth rate is proportional to the concentration at the surface c and the diffusion coefficient D, which scale as T^{-1} and $T^{1.5}$, respectively. Growth rate is expected (and found) to be linear with respect to inlet group-III mole fraction (or flow rate).

Such a simple model, which captures the important physical chemistry of the system but is very easy to evaluate numerically, is ideal to use as a compact "virtual reactor." This virtual reactor can form the basis of advanced process control strategies, e.g., model-based process control, and process design. In this case, the model would be calibrated by comparison with growth rates measured by the in situ optical reflectance monitor as described earlier.

VII. DOPING STATISTICS IN THE ALGAAS ALLOY SYSTEM

Advanced device design requires the knowledge of the free carrier concentration associated with a particular dopant concentration in a particular semiconductor alloy at a specified temperature. In particular we are concerned with the computation of the free electron concentration, n, derived from a fixed Si donor dopant concentration, N_D, in an AlGaAs alloy of fixed AlAs mole fraction, x. The calculation of n is complicated by band structure effects and the existence of a lattice instability for some x which allows a tetrahedrally coordinated donor atom to assume a trigonally bonded interstitial configuration. In the following an attempt is made to describe the physical situation which must be described and steps taken toward resolving some of the outstanding issues with this problem.

In the simplest case we assume that only low doping levels are of interest so that the effects of impurity band formation and conduction band tailing may be neglected. In this case, Boltzmann statistics would be applicable assuming only hydrogenic impurity states are involved. Let us consider the effect of the alloy band structure on hydrogenic impurity states. For $x \leq 0.43$ AlGaAs has a direct band gap at Γ.[17] For $x \geq 0.43$ the alloy is indirect with the conduction band minimum at X.[18] Near the cross-over at $x = 0.43$ the L conduction band minimum is within less than about 50 meV of the Γ and X minima. The donor binding energy of GaAs is well known to be $E_{D\Gamma} \sim 5$ meV. Assuming ellipsoidal energy surfaces at L and X one can estimate $E_{DL} \sim 10$ meV and $E_{DX} \sim 30$ meV. In the virtual crystal approximation E_{DG} can be expected to increase to approximately 10 meV in AlAs while E_{DL} and E_{DX} remain approximately constant. In reality, both the L and X points are nonparabolic in the transverse and longitudinal masses, respectively. This derives from the lack of inversion symmetry in compound semiconductors. The lack of inversion symmetry induces what is referred to as a "camel's back" structure and significantly complicates the computation of the theoretical hydrogenic ground state. To further complicate the theoretical picture the depth of the hydrogenic E_{DX} is comparable to the optical phonon energy. In this case a position dependent permittivity, $\varepsilon(r)$ must be used to properly describe the localized behavior of the 1S ground state.

Investigation of nominally hydrogenic donor states in AlGaAs near the Γ-X cross-over implies the existence of an A_1 symmetry state which appears to track the L band and has a depth of $E_D(A_1) \approx 60$-70 meV.[19] Although the A_1 symmetry is correct for an L derived hydrogenic state it is too deep to be a hydrogenic state unless one invokes central cell effects. Alternatively, the Si atom induces an A_1 symmetry "host like" state which is predicted by tight binding theory to fall about 100 meV below the L band throughout AlGaAs alloys system. These two description are essentially the same because the ad

---

[17] C. Bosio, J. L. Staehli, M. Guzzi, G. Burri, and R. A. Logan, Phys. Rev. B **38**, 3263 (1988).

[18] M. Guzzi, E. Grilli, S. Oggioni, J. L. Staehli, C. Bosio, and L. Pavesi, Phys. Rev. B **45**, 10951 (1992).

[19] R. Dingle, R. A. Logan, and J. Arthur, J. R., In C. Hilsum (Ed.), Gallium Arsenide and Related Compounds, 33a (pp. 210). Edinburgh, Scotland: The Insitute of Physics (1976), T. N. Morgan, Phys. Rev. B **34**, 2664 (1986).

hoc introduction of a central cell potential in a hydrogenic model imitates the first-principles physics of the tight binding model.

If the picture of donor levels in AlGaAs were completely described by the transition from $E_{D\Gamma}$ to $E_D(A_1)$ to E_{DX} then a mathematical model would be relatively straightforward. The significant limitations to the interpretation of experimental data would be the accuracy of our description of the conduction band and the inclusion of dopant interactions at high doping levels. Unfortunately, in the composition range $0.22 \leq x \leq 0.8$ the dopant atoms are metastable with respect to tetrahedral coordination and relax to a negatively charged trigonally bonded interstitial configuration referred to as the DX state. The DX state is the ground state in the specified composition range. It is a highly localized level, deeper than any of the tetrahedrally coordinated donor states. Most importantly, it is sensitive to the local atomic environment of the donor atom. In the case of Si doping in AlGaAs, formation of the DX configuration involves the breaking of a Si-As nearest neighbor (NN) bond with the capture of an electron. The Si atom moves away from the released As atom along the broken bond axis passing through the plane of the three As atoms to which it remains bonded. It comes to rest in an interstitial space with three neighboring (Ga,Al) atoms. The DX energy level depends strongly on the number of Al atoms (0 - 3, four configurations) surrounding it. Since the Si-As bond breaking is not known to be sensitive to the second nearest neighbors (2NN) then any given Si atom could potentially end up in any of four different energy levels.

The situation for Si doped AlGaAs is illustrated in Figure 7. The variation of the conduction bands is shown relative to the vacuum level using the GaAs valence band maximum as the energy zero. If shown, the valence band maximum of the alloy would vary as $E_{vbm} = -0.55x$. The greatest uncertainty is associated with the variation of the L band. The hydrogenic donor states associated with Γ and X are shown as short dashed lines. A true hydrogenic L donor state would never appear as a ground state for the band structure shown. The deep A1 donor state is shown as a long dash line and located according to photoluminescence data. The DX levels (denoted DX_j, $j = 0, 1, 2, 3$) are indicated as chain lines. In AlGaAs doped with a group IV element it is statistically inevitable that some fraction of the Si atoms will be able to access only one of these levels, and others will be able to access all of them.

Consider now the situation for the calculation of the free electron concentration in a 40% alloy. In this case, any Si atom could be in any one of *five distinct states*, $E_D(A_1)$ or one of the four DX levels. The energetic depth of *none of these levels* is amenable to quantitative theoretical treatment. To try to simplify the situation somewhat, consider the use of a group VI donor such as Te. Occupying an As site, the DX state energy levels are determined by the NN group-III atom. However, the number of possible configurations available to form DX levels is determined by four NN atoms rather than twelve 2NN, atoms which simplifies the statistics. On the other hand, the description of the hydrogenic E_{DX} level is complicated by the need to include a valley-orbit interaction term. The effect of the valley-orbit interaction is to split the triply degenerate T_2 ground state, characteristic of a group-VI donor, into a deeper A_1 state and a doubly degenerate E

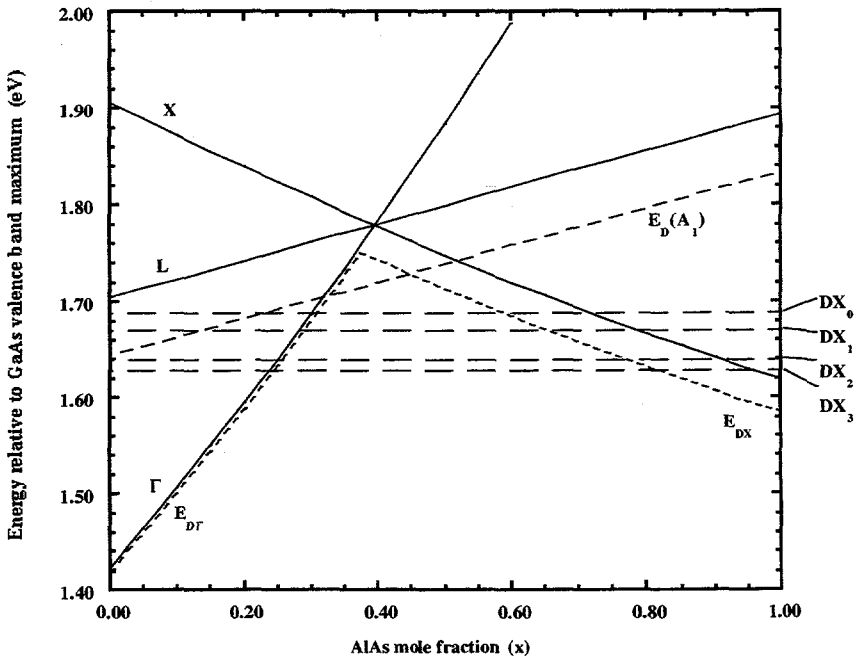

Figure 7. Energy bands and Si donor states in AlGaAs. The energy levels are show relative to the vacuum level with the GaAs valence band maximum as the energy zero. Energy bands are shown as solid lines, tetrahedrally coordinated Si states as dashed lines, and trigonally coordinated donor states (DX states) as chain lines.

symmetry state at about the energy of the T_2 hydrogenic state. Because it is possible tomeasure the A_1-E splitting and calculate the T_2(E) hydrogenic levels beginning with a description of the AlGaAs:Te system, as opposed to AlGaAs:Si, was assumed to be the most reasonable approach to the donor statistics problem.

The first step in the analysis was to evaluate the literature data for AlAs:Te to determine E_{DX}. The value derived from the Hall effect and photoionization was 45 meV for the ground state while the A_1-E splitting was estimated to be about 20 meV.[20] The depth of the E level should, theoretically, be at least 35 meV, which implies $E_{DX} \geq 55$ meV. For AlAs:Si the Hall effect EDX is 57 meV,[21] which should correspond to the depth of the E level and implies that the A level in a similarly doped AlAs:Te sample should be closer to 80 meV.

Using electronic Raman scattering on existing samples of AlGaAs and AlAs doped with Te (in collaboration with NREL), the A_1-E splitting was directly measured to be 23 meV. Evaluation of E_{DX} has not yet been performed due to the unavailability of appropriately doped samples. Without a good doping level dependent study of both AlAs:Te and AlAs:Si to determine E_{DX} in AlAs to better than the existing 50% uncertainty, constructing an alloy model is unlikely to be profitable.

---

[20] A. J. SpringThorpe, F. D. King, and A. Becke, J. Electron. Mat. **4**, 101 (1975), J. E. Dmochowski, L. Dobaczewski, J. M. Langer, and W. Jantsch, Phys. Rev. B **40**, 9671 (1989).

[21] N. Chand, T. Henderson, J. Klem, W. T. Masselink, R. Fischer, Y.-C. Chang, and H. Morkoç, Phys. Rev. B **30**, 4481 (1984).

DIRECTIONS FOR THE DEVELOPMENT OF A PREDICTIVE FREE ELECTRON MODEL FOR AlGaAs

Assuming that the energy levels and configuration statistics are known for a particular AlGaAs alloy it should be possible to estimate nondegenerate free carrier concentrations for temperatures above about 130 K for samples in the dark. The simplest approach would be to use Boltzmann statistics and assume parabolic energy dispersions for each of the relevant conduction band minima.[22] The next level of sophistication would be to include nonparabolicity in the conduction band at the X.[23] This dramatically increases the calculated density of states for given effective mass parameters. For nondegenerate statistics parabolic band minima may be described by a temperature independent effective density of states represented as a delta function at the band edge. Nonparabolicity introduces a temperature dependence into an effective density of state representation.

The next level of sophistication requires a statistical analysis of the distribution of lowest energy configurations in alloy configuration in which a DX state is possible.[24] A donor atom may be able to relax into several different DX configurations and at temperatures above 130 K it should be assumed that the donor has sufficient thermal energy to achieve the lowest attainable configuration within a reasonable time span.[25] A difficulty at this time is the ongoing controversy as to the energy levels associated with the distinct DX alloy configurations. It is important to observe that the vast majority of past analyses have assumed that all donor atoms can achieve the same ground state energy. This is incorrect. With the exception of the binary endpoint compounds there will always be a spectrum of ground state energies dependent upon the presumably random distribution of local environments. Such an analysis also allows for the application of the proper statistics according to whether a DX ground state is, or is not, allowed. Donor atoms with only hydrogenic ground states will capture, at most, one electron and positive U statistics apply. DX ground states which capture two electrons must be described by negative U statistics.[26]

Extension of the analysis of the free electron concentration to degenerate doping conditions is problematic. A good solution to this problem does not exist even for donors with simple hydrogenic ground states.[27] However, tractable approximations do exist.[28] Such models attempt to describe overlap of the wavefunctions of electrons localized on the donor atoms and the tailing of the band edge due to the attractive screened Coulomb potential of the ionized donors. The introduction of negative U DX centers introduces a new complexity. Although the two electron ground state is assumed to be sufficiently localized to avoid wave function overlap, the ground state configuration is now negatively charged. This introduces repulsive Coulomb perturbations in the conduction band edge and should shift the effective band edge away from the impurity level leading to an anti-band tailing effect. For compositions for which DX and hydrogenic levels are nearly degenerate and large numbers of both configurations may exist the combined

---

[22] N. Chand et al., ibid.

[23] A. A. Kopylov, Sol. St. Commun. **56**, 1 (1985).

[24] T. N. Morgan, J. Electron. Mat. **20**, 63 (1991).

[25] Z. Su, and J. W. Farmer, Appl. Phys. Lett. **59**, 1746 (1991).

[26] D. C. Look, Phys. Rev. B **24**, 5852 (1981).

[27] C. Butulay, I. Al-Hayek, and M. Tomak, Phys. Rev. B **56**, 15115 (1997).

[28] T. F. Lee, and T. C. McGill, J. Appl. Phys. **46**, 373 (1975).

effect of mixed attractive and repulsive Coulomb centers should have a significant effect on the apparent activation energy. A theoretical description of this effect has yet to appear in the literature.

In summary, it is theoretically possible to generate a model of the free electron density for the AlGaAs alloy system. Indeed, very simple models can be found in the literature. However, given the poor understanding of the hydrogenic levels associated with the X minima in indirect alloys these descriptions are empirical at best. A substantial amount of experimental work with the high Al mole fraction alloys will be required to generate an improved description of these materials.

Intentionally Left Blank

VIII. MOCVD REACTOR AUTOMATION AND CONTROL ARCHETECTURE

Two MOCVD reactors have been built and/or modified to perform computer-controlled, recipe-driven growth of multilayered structures with designed bandgaps. The control software of the two systems, (an Emcore commercial reactor and a Sandia-designed research reactor) share similar architectures. A schematic of the Sandia system's control software is shown at right. The open and flexible design of the computer control allows the inclusion of additional growth diagnostics to aid in monitoring and evaluating the growth process.

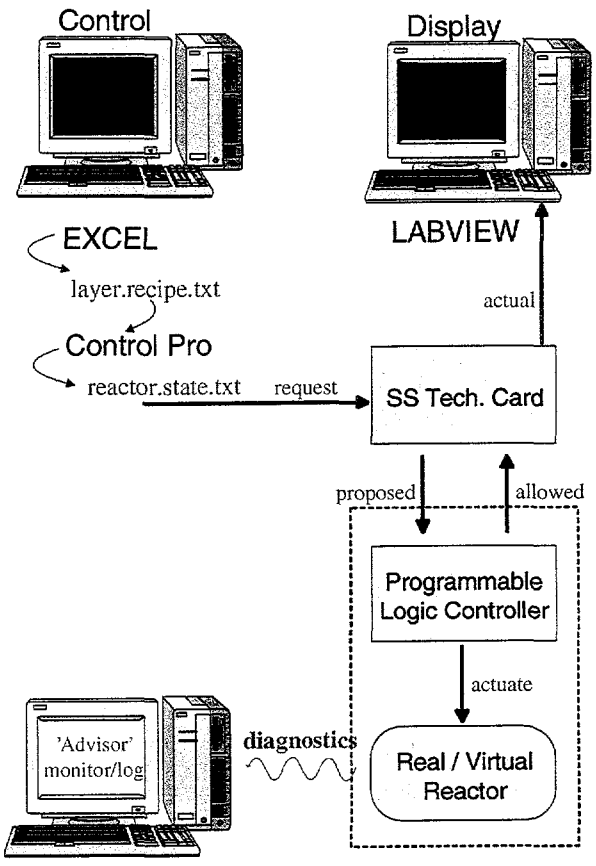

Figure 8. Schematic of the recipe execution process in the MOCVD reactor. An autonomous monitoring program, "Advisor," determines growth rates in situ.

The individual steps in the growth of a device are defined by a growth "recipe" written by the grower using a Microsoft Excel spreadsheet. This text-based recipe contains commands which call for changes in gas flow rate or species, changes of temperatures, enforced "wait" periods, etc. In the case of the Sandia reactor, these descriptive commands are translated by a Visual Basic macro into a reactor-specific instruction set which is executed by a commercial control program labeled "Control Pro" in Figure 8. Each hardware-specific instruction is presented, via a device-mapped interface card, to a reactor-specific programmable logic controller (PLC). The PLC checks that the command is safe to execute in the reactor's current state, and then delivers the instruction to the specified hardware device (e.g., flow controller, heater, valve). In the case of the Sandia-designed reactor, an autonomous computer running a National Instruments' LabVIEW-based program, independently monitors and displays the changing state of the reactor hardware.

Intentionally Left Blank

In parallel with the computer-controlled execution of the growth recipe, an independent diagnostic process, labeled "Advisor" in Figure 8, monitors and records the reflectance of laser light from the growing surface as a function of both wavelength and time. The modulations in the intensity of this surface-reflected light provide a real-time measure of the layer thickness resulting from the on-going incorporation of atoms into the surface from the vapor phase, as described in Section IV. Analysis of this reflectance data provides an independent measure of the "as-grown" layer thickness, in contrast to the "recipe-predicted" layer thickness. With such information, subsequent recipe creation can be re-calibrated to the reactor's empirically-determined response, and consequently finer control of the dimensions of grown structures can be achieved.

IX. VIRTUAL REACTOR ARCHITECTURE

Ideally, any disparity between the device structure defined by the growth recipe and the "as-grown" structure would be below a threshold necessary to impact the desired electronic properties of the fabricated device. However, as structures become smaller and more complicated, the acceptable margin of error in each step of the growth process also becomes smaller. Moreover, as the complexity of the fabricated device increases, the investment in time and resources for its creation also increases, arguing for a capability to, at a minimum identify the parameter(s) responsible for any deviations from a design's specification, and optimally, to take corrective actions in a growth recipe before its completion.

In order to achieve the ability to identify, and even correct, small, slow drifts in the calibration constants of the physical reactor and its ensemble of transducers, we are integrating the results of this LDRD project to construct a software package that encompasses: (1) the recipe execution and reactor control functions of the existing software, (2) the diagnostic capabilities of the "Advisor" reflectance measurement and analysis program, and (3) the physics-based simulation capabilities of the models such as the one described in Section VI.

By simultaneously executing the growth recipe in the real reactor, modeling the growth recipe in a "virtual" reactor, and sharing a common pool of information about the state of each reactor and supporting diagnostics, differences in the observed and simulated system parameters can be identified. These differences may then suggest reactor simulations that reproduce the observed growth effects and thus identify parameters or calibrations that have drifted. Such information can be used to recalibrate future growth runs, or more boldly, to adjust the remainder of a currently executing recipe in order to compensate for this drift and still achieve the desired device performance.

Intentionally Left Blank

The multiple, independent tasks of recipe interpretation and execution, system control, diagnostic measurement and analysis, and process simulation are being integrated into a single, interdependent control structure using National Instrument's BridgeVIEW industrial automation graphical programming environment. As depicted in Figure 9, the initial device design is performed in an Excel-based spreadsheet. The layer-based design is then converted to a machine-specific set of hardware instructions and saved as a text recipe file. This recipe file can then be read and executed by the BridgeVIEW based "Virtual Reactor" program. Each independent task can be executed as a multi-threaded, autonomous process, but can still access the data (via Microsoft-standard OLE process control) of all other processes. Subprocesses execute C and Fortran dynamic link libraries which in turn can access external software packages such as CHEMKIN-based code. Data is retrieved, shared and logged, and a graphical user interface accesses the entire process. Code developed in this package can be ported to Win95, NT, Mac, and UNIX platforms. The reactor-specific features of the program are localized in the layer description-to-machine instruction macro in Excel, the device-mapping of the interface card, and a data array (the "System Constants Array") that describes the physical constants of the reactor within the program. A graphical user interface displays the status of the recipe execution in the real reactor, and also the status of the simulations used to model the real reactor's response. A snapshot of the front panel interface is shown in Figure 10.

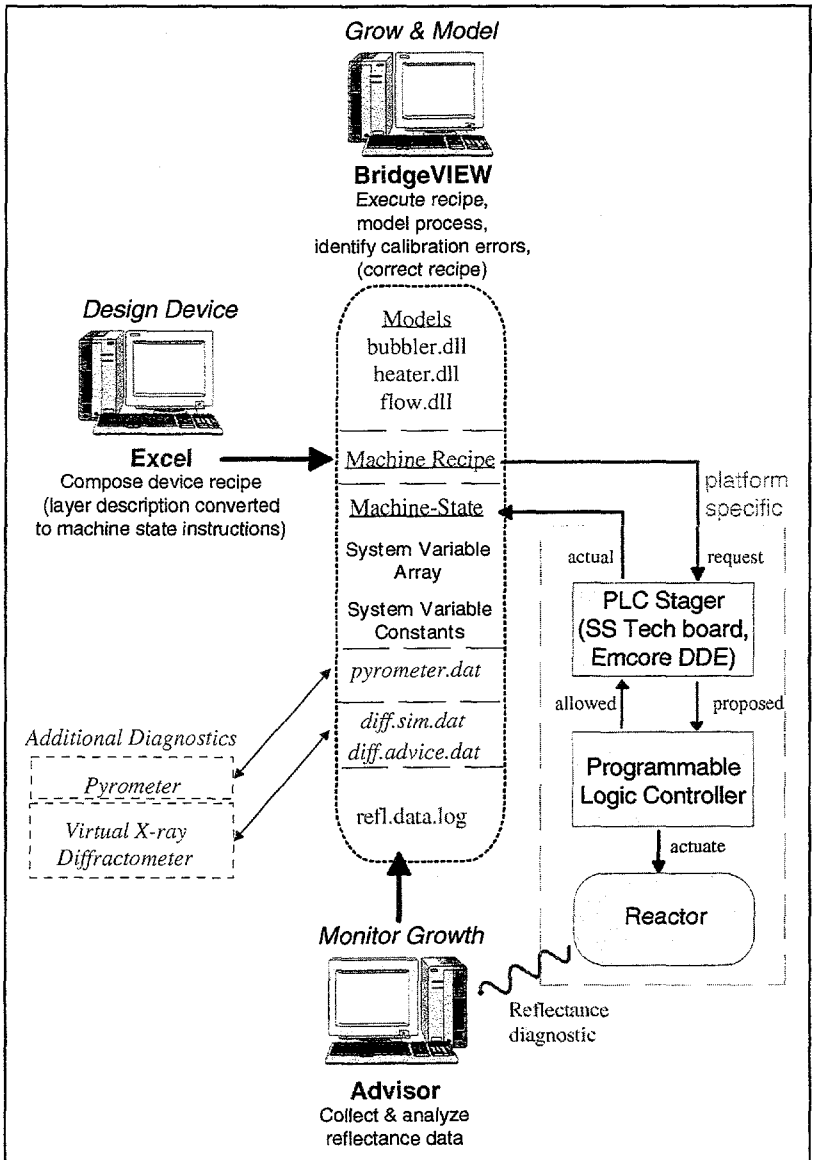

Figure 9. Schematic of the functional processes of the

Intentionally Left Blank

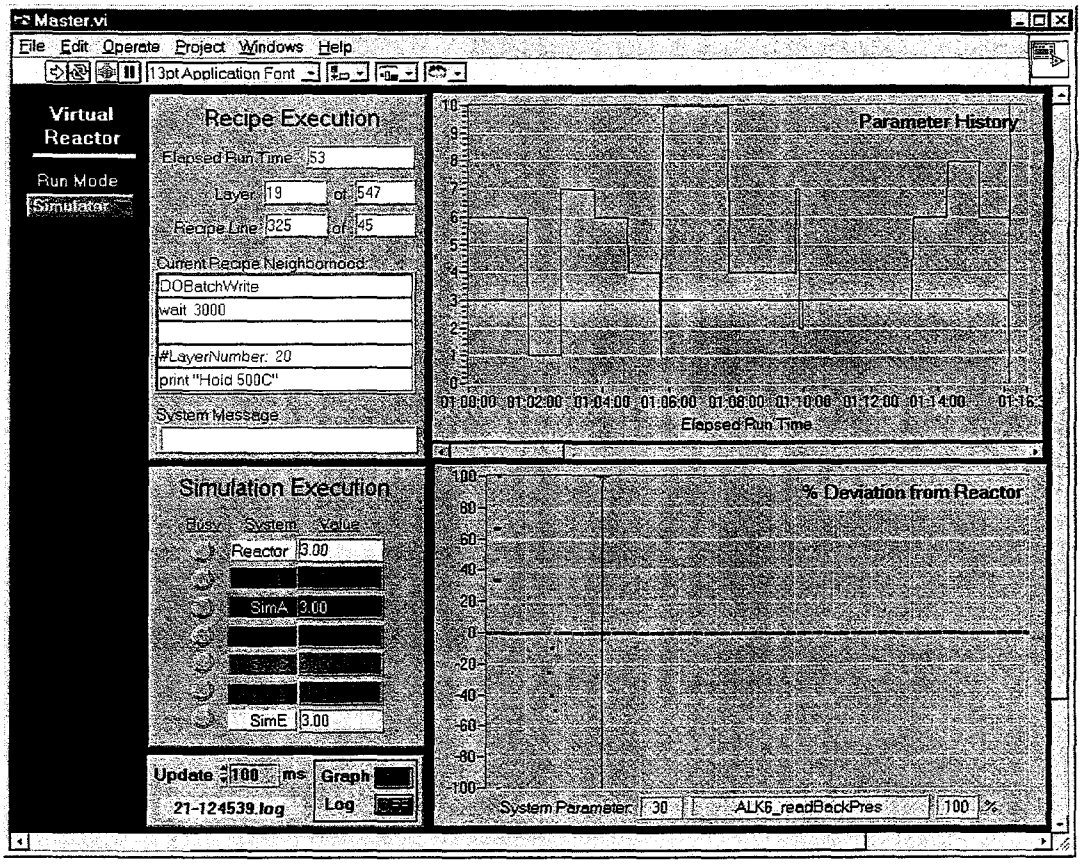

Figure 10. Snapshot of the front panel of the Virtual Reactor control and simulation system.

Intentionally Left Blank

Within the "Virtual Reactor" program, the real and simulation reactors are each described by two sets of data, an array of **system constants** which describe the unvarying parameters of the system (e.g., lengths and diameters of tubing, valve response times, platen diameter and inlet height), and an array of **system variables** that reflects the intentionally changeable parameters in the system (e.g., flow rates of particular gases, valve status, platen temperature). One purpose of the system constants array is to allow the program to be ported to other physical reactors without a major revision of the program code. Additionally, by representing the most detailed physical aspects of the system, more subtle effects of recipe execution are open to future simulation by the virtual reactor. (For example, some existing data suggest that gas flow transients due to finite valve closure times in conjunction with a run line's fixed conductance may affect interface widths under some growth conditions.)

The real reactor and simulations share a common system constants array. However, each reactor possesses its own system variable array (SVA). Approximately 247 system variables have been identified to date on the Sandia-designed reactor. The contents of the real reactor's SVA reflects the execution of the growth recipe and feedback from transducers and sensors on the real reactor. The contents of the simulations' SVAs also reflect execution of the recipe, but without any sensor feedback (e.g., a command to change the platen temperature is assumed to accomplish its goal per an existing model, and no thermocouple feedback occurs.) For a perfect simulation of reality, the difference between the reactor SVA and each simulation's SVA would equal zero. A graph of the percent deviation of each simulation's SVA from the real reactor's SVA is plotted in the lower right quadrant of the program's user interface. From this plot, it becomes immediately apparent which simulation variables are diverging from reality. The time-history of a specific variable can be plotted in the upper right quadrant of the front panel by mouse-clicking on the variable's channel. Assuming that the fidelity of the simulation's performance to the real reactor has previously been established, (so that we can assume that the current disagreement results from a variation in one of the real reactor's properties), the program can launch up to five "test" simulations to try to replicate the variable's deviation in time. The "Virtual Reactor" acts as the representative of the best test simulation results; the five test simulations can be thought of as scratch pads which seek out and identify "errant variables". The simulation with the least deviation from reality is always preserved in the model labeled "Virtual" until a better simulation arises.

The launching of one of the test simulations can arise from user intervention or automatically when a variable strays outside a pre-defined allowable variance with reality. The goal of a test simulation is to find agreement with reality; once it has replicated the current situation, only then are corrective actions to the remaining recipe considered. While the test simulations search to replicate the existing deviation, the recipe execution continues undisturbed in the real reactor unless or until a pre-programmed "permission to hold" is encountered in the recipe. Upon encountering a "permission to hold," the program will exert its full efforts to reconcile the virtual reactor with the real reactor. This is done by the five test simulations ranging over a widening parameter space.

The five test simulations survive from one recipe step to another in a "survival of the fittest" mode. As long as the contents of the test simulations' SVAs do not exceed the preset Sim Survival Range setting, the simulation continues to execute recipe steps as they become available. However, if a given simulation begins to deviate further from the reactor's SVA than the Sim Survival Range, it dies off and is replaced with the test simulation with the least deviation from the reactor's SVA.

By implementing parallel simulations of the growth process, small drifts in reactor performance or calibration can be identified and corrected. Once the fidelity of the simulations are established, a virtual reactor also permits recipes to be tested on the desktop before being actually grown.

X. SUMMARY

A variety of experimental and modeling tools have been used to improve the efficiency, reliability, and yield in fabricating compound semiconductor thin films. This effort is founded on a modular and configurable process automation system that serves as a backbone allowing integration of process-specific models and sensors. We have developed and integrated MOCVD- and MBE- specific models in this system, and demonstrated the effectiveness of sensor-based feedback control in improving the accuracy and reproducibility of semiconductor heterostructures. In addition, within this framework we have constructed "virtual reactor" models for growth processes, with the goal of greatly shortening the epitaxial growth process development cycle.

UNLIMITED RELEASE

DISTRIBUTION:

1		Hong Hou Emcore Corp. 10420 Research Rd SE Albuquerque, NM 87123
1		R. J. Kee Division of Engineering Colorado School of Mines Golden, CO 80401
1		K. P. Killeen Solid State Technology Laboratory 3500 Deer Creek Rd. 26M-7 Palo Alto, CA 94303-0867
1	1100	S. T. Picraux, MS0360
1	1113	R. M. Biefeld, MS0601
1	1126	K. Baucom, MS0601
1	1126	W. G. Breiland, MS0601
20	1126	M. E. Coltrin, MS0601
1	1126	J. R. Creighton, MS0601
1	1126	J. Han, MS0601
1	1126	H. K. Moffat, MS0601
1	1126	C. C. Willan, MS0601
1	1126	J. Y. Tsao, MS0601
1	1711	A. A. Allerman, MS0603
1	1711	J. F. Klem, MS0603
1	1711	T. J. Drummond, MS0603
1	1711	P. Esherick, MS0603
1	9343	K. M. Horn, MS1167
2	4916	Technical Library, MS0899
1	15102	Review & Approval Desk, MS0619
1	8940-2	Central Technical Files, MS9018